Insight into restructuring of Pd-Au nanoparticles using EXAFS

Alexey Boubnov[a], Janis Timoshenko[b], Cody J. Wrasman[c], Adam S. Hoffman[a], Matteo Cargnello[c], Anatoly I. Frenkel[b,d], Simon R. Bare[a,*]

[a] SLAC National Accelerator Laboratory, Menlo Park, CA, 94025, United States
[b] Department of Materials Science and Chemical Engineering, Stony Brook University, Stony Brook, NY, 11794, United States
[c] Department of Chemical Engineering and SUNCAT Center for Interface Science and Catalysis, Stanford University, Stanford, CA, 94305, United States
[d] Chemistry Division, Brookhaven National Laboratory, Upton, NY, 11973, United States

ARTICLE INFO

Keywords:
Dilute alloy
Palladium
Gold
Catalyst
Multi-edge EXAFS
Structural model

ABSTRACT

We acquired Pd K-edge and Au L_3-edge EXAFS spectra of two libraries of titania-supported Pd-doped Au nanoparticle catalysts representing the as-prepared and post-catalysis state. The nanoparticles have narrow particle size distributions, in the range 2.8–6.6 nm, and were synthesized to preferentially locate the palladium atoms on the surface of a gold core, with Pd mole fractions of 1.4–38%. EXAFS spectra of both the as-prepared samples and post-catalysis Pd-Au particles were collected and modeled. EXAFS refinement of all samples showed contributions from both Pd-Au and Pd-Pd scattering paths, revealing that Pd and Au components alloyed together. Pd was in a partially oxidized state as evidenced by a Pd-O scattering contribution, unlike Au. Overlaying measured coordination numbers from the libraries with predicted values, using models of surface and bulk alloying, showed that Pd restructures among Au as a result of exposure to the reaction conditions.

1. Introduction

Recently, catalytic hydro-oxidation (Wrasman et al., 2018) has proven effective in complete conversion of short-chain hydrocarbons with high selectivity, e.g. the selective oxidation of 2-propanol to acetone, potentially providing a pathway for other selective oxidation reactions. The reaction utilizes a feed of hydrocarbon, oxygen and hydrogen over a single-atom alloy catalyst, where a single platinum-group metal atom (e.g. Pd) on a coinage metal surface (e.g. Cu or Au) dissociates hydrogen, but not oxygen. The dissociated hydrogen forms a peroxide with molecular oxygen from the gas phase, subsequently oxidizing the organic molecule, e.g. alcohol to acid (Nijhuis et al., 1999).

EXAFS modeling was used to gain insight into the location of Pd in or on the surface of the Au nanoparticles after the synthesis and post-catalysis, to gain information on the structural stability of these catalysts. Applying modeling of bulk and surface atoms to the EXAFS analysis allowed the distribution of Pd among Au to be characterized, for which supervised machine learning is applied and EXAFS data serves as training sets for the artificial neural network (Timoshenko et al.). Given statistical uncertainties on the EXAFS analysis, the use of structural models from the analysis of sample libraries, rather than from a single sample, allows trends in the data to be readily observed.

Here, EXAFS data from the as-prepared catalysts, with 3.7–6.6 nm particle size and 3.0–38% molar Pd fraction, were collected at the Stanford Synchrotron Radiation Lightsource (SSRL), while EXAFS data from the post-catalysis samples, with 2.8–5.5 nm with Pd molar fractions of 1.4–10.5%, were recorded at the Advanced Photon Source (APS). The data were analyzed independently by the two groups, followed by a joint interpretation.

2. Methods

Colloidal Pd-Au nanoparticles (NPs) were prepared, as previously described, by depositing Pd on the surface of initially synthesized Au NPs using a modified seed-mediated process (Cargnello et al., 2015). The Pd-Au NPs were supported on TiO_2 (P25) to obtain a weight loading of 0.5% (samples 1–8 in Table 1). Post-catalysis samples 9–16 were tested for catalytic performance in a flow of 1% CH_4 + 1% O_2 + 1% H_2, balance He for 2 h at 300 °C. Transmission electron microscope images of samples 1–8 are shown in Fig. S1 and for samples 9–16 in the as-prepared state in reference (Wrasman et al., 2018).

EXAFS spectra of samples 1–8 were measured at APS beamline 12-BM-B at the Pd K-edge (24350 eV) and the Au L_3-edge (11919 eV) using the Si(111) double-crystal monochromator. Analogous measurements of samples 9–16 were conducted at the Pd K-edge at SSRL at beamline

* Corresponding author.
E-mail address: srbare@slac.stanford.edu (S.R. Bare).

Table 1
Nanoparticle size and Pd fractions of Pd-Au particles in the as-prepared samples 1–8 and post-catalysis samples 9–16.

Size	Sample No.	$< d >$ [nm]	x_{Pd} [mol.%]
Small (APS)	1	3.7 ± 0.7	4.4
	2	3.9 ± 0.6	14.8
	3	4.3 ± 0.8	24.4
	4	4.4 ± 0.7	38.0
Large (APS)	5	6.6 ± 0.6	3.0
	6	5.1 ± 0.4	4.5
	7	5.3 ± 0.4	11.8
	8	5.7 ± 0.3	20.2
Small (SSRL)	9	2.8 ± 0.4	1.4
	10	2.8 ± 0.4	4.1
	11	2.8 ± 0.4	7.0
Medium (SSRL)	12	4.3 ± 0.4	3.2
	13	3.8 ± 0.4	5.1
	14	4.4 ± 0.4	10.5
Large (SSRL)	15	5.4 ± 0.5	1.8
	16	5.5 ± 0.5	6.9

7-3, using a Si(220) double-crystal liquid nitrogen-cooled monochromator. The samples were pressed into self-supporting pellets and data were recorded in fluorescence mode at room temperature using a 13-element Ge detector (Canberra) at APS and a 32-element Ge detector (Canberra) at SSRL. To improve the signal-to-noise ratio, 7–15 scans of each sample were collected. Pd foil, PdO and Au foil were used as reference compounds for data fitting. The metallic foils, scanned concurrently with the samples, were used as energy-calibration standards.

The raw data were processed using the FEFFIT code and the Athena and Artemis interfaces of the Demeter software package (Ravel and Newville, 2005). The spectra were energy-calibrated, merged and normalized. The EXAFS spectra were extracted in *k*-space, Fourier-transformed on the range k = 2.4–12.0 Å^{-1} and fitted in *R*-space between 1.2 and 3.0 Å for samples 1–8 at the Pd K-edge. Corresponding ranges were k = 3.0–12.0 Å^{-1}, R = 1.2–3.5 Å (samples 1–8, Au L_3-edge) and k = 3.0–11.5 Å^{-1}, R = 1.3–3.3 Å (samples 9–16, Pd K-edge). At the Pd K-edge, Pd-O, Pd-Pd and Pd-Au shells were refined and at the Au L_3-edge, the Au-Pd and Au-Au shells. Phase shifts and amplitudes for relevant back-scattering paths were calculated using FEFF8 (samples 1–8) and FEFF6 (sample 9–16) (Ankudinov et al., 1998) from crystallographic information files of PdO, Au_3Pd *fcc*-alloy and Au metal. EXAFS modeling was carried out taking into account k^1 and k^2-weighting for samples 1–8 and k^1, k^2 and k^3-weighting for samples 9–16. Fitting of all spectra for samples 1–8, as well as for samples 9–16, was performed simultaneously. Electronic amplitude reduction factors S_0^2 was determined as 0.65 ± 0.05 for the Pd K-edge from fitting Pd foil and 0.90 ± 0.04 for the Au L_3-edge from fitting Au foil at APS and 0.78 ± 0.04 (Pd K-edge) at SSRL.

3. Results and conclusions

XANES and EXAFS spectra are shown in Fig. 1 for samples 1 (as prepared) and 13 (post-catalysis) with similar size and Pd content from both groups, while complete data sets are presented in Fig. S2–S9 and Tables S1 and S2 in Supporting Information. XANES spectra at both the Pd K-edge and Au L_3-edge show a metallic state of both elements, Fig. 1 (a). EXAFS spectra of all samples are high quality, and analyzable up to a *k*-value of 12 Å^{-1}, Fig. 1 (b). The Fourier-transform EXAFS spectra are dominated by detectable scattering contributions in the 1–2 Å and 2–3 Å ranges in *R*-space, Fig. 1 (c).

Table 2 shows that Pd in sample 13 (post-catalysis) was mainly surrounded by Au and to a smaller degree by Pd and O. The latter two contributions were not observed in as-prepared sample 1. Au-Au contribution in sample 1 was high as expected, with a small amount of Au-Pd present. To determine the distribution of Pd among Au, structural models predicting coordination numbers (CNs) are required, to compare with experimentally determined ones.

To model the location of Pd among Au on a particle length scale based upon the obtained CN, structural models representing bulk-alloying and surface-alloying of Pd with Au were derived, Eqs. (1) and (2) and Eq. (3), respectively. Similar predictive models have been developed for random-alloyed (Frenkel, 2012) and core-shell (Knecht et al., 2008) bimetallic nanoparticles. Bulk alloying assumed a homogeneous mixture of the two metals and CNs of Pd-Pd and Au-Pd were calculated using the binomial distribution as a function of the Pd loading (x_{Pd}):

$$CN_{Pd-Pd} = \sum_{l=2}^{13}\sum_{k=l}^{13}\binom{13}{k}x_{Pd}^{k}(1-x_{Pd})^{13-k} \quad (1)$$

and

$$CN_{Au-Pd} = \sum_{l=1}^{12}\sum_{k=l}^{13}\binom{13}{k}x_{Pd}^{k}(1-x_{Pd})^{13-k} \quad (2)$$

In an *fcc*-lattice, based on a cluster of 13 atoms with a Pd central atom and 12 nearest-neighbors, $CN_{Pd\text{-}Pd}$ = 1 means that there are 2 Pd among the 13 atoms, that is x_{Pd} = 2/13 = 15.4%. For the same x_{Pd}, $CN_{Au\text{-}Pd}$ would be 2, i.e. 2 Pd neighbors next to a central Au. The nanoparticles were assumed to be "bulk-like" based upon particle sizes above ca. 3 nm and by the sum $CN_{Au\text{-}Au}$ + $CN_{Au\text{-}Pd}$ approaching 12 (Borowski, 1997). $CN_{Au\text{-}Au}$ and $CN_{Pd\text{-}Au}$ were determined by subtracting $CN_{Pd\text{-}Pd}$ and $CN_{Au\text{-}Pd}$ from 12. The four coordination numbers are depicted as solid lines in Fig. 2 (a) and (b) with experimental data of the as-prepared and post-catalysis samples.

The other model was surface-alloying, where Pd was assumed to be confined to the outer monolayer. Thus the maximum number of neighboring atoms around a Pd central atom is 9, i.e. 6 surface atoms (either Pd or Au) and 3 sub-surface Au. $CN_{Pd\text{-}Pd}$ and $CN_{Pd\text{-}Au}$ were calculated analogous to those for the bulk-alloy model, but as a function of the surface concentration of Pd, x_{Pd}/D, where dispersion D is the

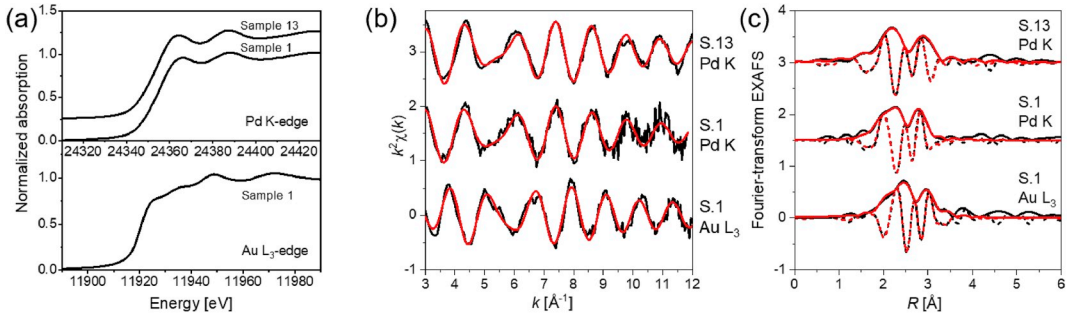

Fig. 1. (a) XANES, (b) EXAFS in *k*-space and (c) Fourier-transform EXAFS of samples 1 and 13. Black lines: experimental data, red lines: fit. Fourier-transform solid lines: magnitude and dashes: imaginary part. Results for all samples are contained in Fig. S2–S9. (For interpretation of the references to colour in this figure legend, the reader is referred to the Web version of this article.)

Table 2
Bond distances, coordination numbers and mean thermal displacement terms refined from EXAFS of samples 13 (Pd K-edge) and 1 (Pd K and Au L_3-edge). Results for all samples are contained in Tables S1 and S2.

Sample	Path	d [Å]	CN	σ^2 [Å^2]	ΔE_0 [eV]	R-factor [%]
13 (SSRL)	Pd-O	1.98 ± 0.02	0.4 ± 0.4	0.011 ± 0.001	−1.1 ± 0.4	1.2
Pd K	Pd-Pd	2.82 ± 0.02	0.6 ± 0.2	0.003 ± 0.001		
	Pd-Au	2.83 ± 0.00	10.4 ± 0.8	0.009 ± 0.001		
1 (APS)	Pd-O	–	0	–	−4.6 ± 0.2	2.1
Pd K	Pd-Pd	–	0	–		
	Pd-Au	2.81 ± 0.01	14 ± 2	0.011 ± 0.001		
1 (APS)	Au-Pd	2.81 ± 0.01	0.5 ± 0.4	0.011 ± 0.001	4.8 ± 0.2	1.3
Au L_3	Au-Au	2.83 ± 0.00	10.3 ± 0.8	0.009 ± 0.001		

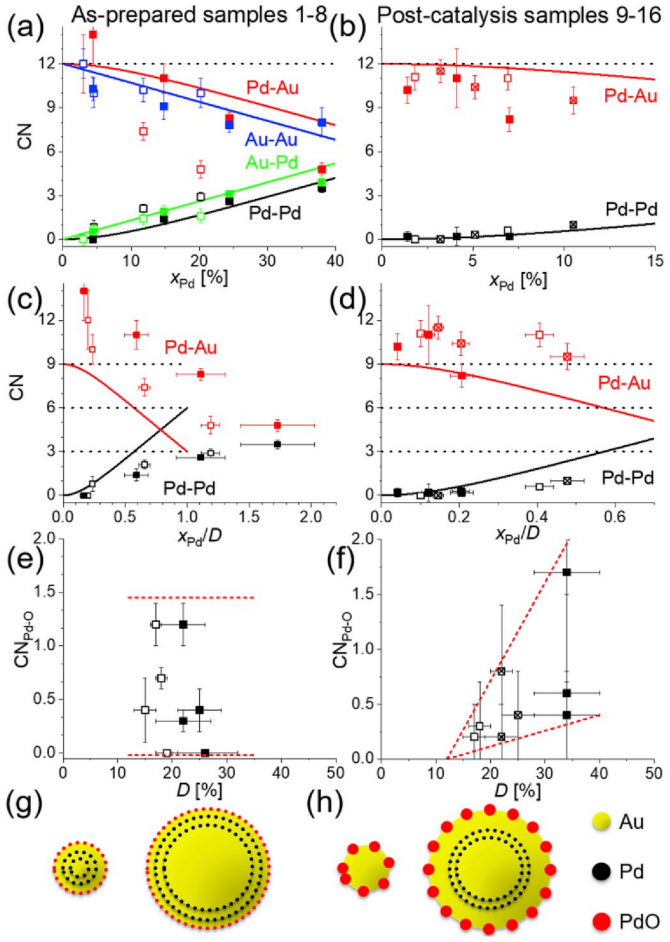

Fig. 2. Experimentally determined coordination numbers for as-prepared and post-catalysis samples matched against models for (a–b) bulk-alloying, (c–d) surface-alloying of Pd and (e–f) dispersion-dependence of surface-oxide formation, red dashed lined outline trends to guide the eye. Legend to size: large (□), medium (⊠) and small (■). Cartoons (g) and (h) depict the distribution of Pd, Au and PdO for small and large particles in samples as-prepared and post-catalysis respectively, consistent with experimental data tested against structural models. (For interpretation of the references to colour in this figure legend, the reader is referred to the Web version of this article.)

fraction of surface atoms to total atoms determined by the relation $D = 0.96\ \text{nm}/ < d >$:

$$CN_{Pd-Pd} = \sum_{l=2}^{7}\sum_{k=l}^{7}\binom{7}{k}(x_{Pd}/D)^k(1 - x_{Pd}/D)^{7-k} \quad (3)$$

and $CN_{Pd\text{-}Pd} + CN_{Pd\text{-}Au} = 9$.

Predicted CNs are shown in Fig. 2 (c) and (d) compared to the experimental data.

For the as-prepared sample data in Fig. 2 (a), $CN_{Pd\text{-}Au}$ for small particles (red full symbols) were high and matched the bulk-alloying model (red line), while $CN_{Pd\text{-}Au}$ for large particles (empty red symbols) were significantly lower and best matched the surface-alloy model in Fig. 2 (c). A higher $CN_{Au\text{-}Au}$ for large than for small particles consistently shows that Au is more associated with Au than Pd in the former. $CN_{Pd\text{-}Pd}$ and $CN_{Au\text{-}Pd}$ are rather low, confirming the homogeneous distribution of Pd, increasing with x_{Pd}. Also, $CN_{Pd\text{-}O}$ in Fig. 2 (e) was independent of dispersion, as expected for surface-confined Pd that would be subject to oxidation. The cartoon in Fig. 2 (g) depicts the Pd distribution derived from the EXAFS analysis, showing a Pd-Au alloy close to the surface of large particles but occupying most of the volume of the small particles.

Post-catalysis samples also showed a low-concentration and partially oxidized Pd, but since they were exposed to reaction conditions prior to measurements, exhibited significant differences to the as-prepared samples. $CN_{Pd\text{-}Au}$ in Fig. 2 (b) and (d) represented structures closer to bulk-alloying for the medium/large particles and surface-alloying for the small, opposite of the tendency observed in the as-prepared state. Furthermore, $CN_{Pd\text{-}O}$ was positively correlated to the dispersion, showing in small particles, a large fraction of Pd is oxidized due to the high surface area, while for large particles, some reduced Pd is retained in the inside of the particle, Fig. 2 (f). This and the inverse effect particle size on bulk/surface-alloying is feasible if Pd close to the surface segregates into islands on the particle surface and oxidizes, as depicted in the cartoon in Fig. 2 (h).

In conclusion, we have shown that the distribution of Pd in Au depends on the chemical history of the samples: as-prepared samples contain highly-dispersed Pd close to the nanoparticle surface, whereas Pd is segregated as larger moieties in the post-catalysis samples. These findings were obtained by comparison of sample libraries with varied particle size and Pd loading, which is important because both these parameters are part of the structural model. The combined effort of two groups analyzing two sample libraries has verified this consistency and gained a broad structural insight into alloying as a function of particle size, composition and chemical environment history.

Acknowledgements

Use of the Stanford Synchrotron Radiation Lightsource, SLAC National Accelerator Laboratory (SLAC), is supported by the U.S. Department of Energy (DOE), Office of Science (SC), Office of Basic Energy Sciences (BES) under Contract No. DE-AC02-76SF00515. Use of the Advanced Photon Source is supported by DOE, SC, BES under Contract No. DE-AC02-06CH11357. A. I. F. acknowledges support by the DOE, SC, BES, under Grant No. DE-FG02-03ER15476. C. J. W. and M. C. acknowledge support from the DOE, SC, BES to the SUNCAT Center for Interface Science and Catalysis. SRB and A.S.H acknowledge support from DOE, SC, BES DOE BES funded Consortium for Operando and Advanced Catalyst Characterization via Electronic Spectroscopy

and Structure (Co-ACCESS) at SLAC. TEM work was performed at the Stanford Nano Shared Facilities, supported by the National Science Foundation under award ECCS-1542152.

Appendix A. Supplementary data

Supplementary data to this article can be found online at https://doi.org/10.1016/j.radphyschem.2019.04.054.

References

Ankudinov, A., et al., 1998. Real-space multiple-scattering calculation and interpretation of x-ray-absorption near-edge structure. Phys. Rev. B 58, 7565–7576. https://doi.org/10.1103/PhysRevB.58.7565.

Borowski, M., 1997. Size determination of small Cu-clusters by EXAFS. J. Phys. IV Fr. 7https://doi.org/10.1051/jp4/1997190. C2-259-C252-260.

Cargnello, M., et al., 2015. Uniform bimetallic nanocrystals by high-temperature seed-mediated colloidal synthesis and their catalytic properties for semiconducting nanowire growth. Chem. Mater. 27, 5833–5838. https://doi.org/10.1021/acs.chemmater.5b02900.

Frenkel, A.I., 2012. Applications of extended X-ray absorption fine-structure spectroscopy to studies of bimetallic nanoparticle catalysts. Chem. Soc. Rev. 41, 8163–8178. https://doi.org/10.1039/C2CS35174A.

Knecht, M.R., et al., 2008. Structural rearrangement of bimetallic alloy PdAu nanoparticles within dendrimer templates to yield core/shell configurations. Chem. Mater. 20, 1019–1028. https://doi.org/10.1021/cm0717817.

Nijhuis, T.A., et al., 1999. Direct epoxidation of propene using gold dispersed on TS-1 and other titanium-containing supports. Ind. Eng. Chem. Res. 38, 884–891. https://doi.org/10.1021/ie980494x.

Ravel, B., Newville, M., 2005. ATHENA, ARTEMIS, HEPHAESTUS: data analysis for X-ray absorption spectroscopy using IFEFFIT. J. Synchrotron Radiat. 12, 537–541. https://doi.org/10.1107/S0909049505012719.

Timoshenko, J., et al., 2019. Probing atomic distributions in mono- and bimetallic nanoparticles by supervised machine learning. Nano Lett. 19, 520–529. https://doi.org/10.1021/acs.nanolett.8b04461.

Wrasman, C.J., et al., 2018. Synthesis of colloidal Pd/Au dilute alloy nanocrystals and their potential for selective catalytic oxidations. J. Am. Chem. Soc. 140, 12930–12939. https://doi.org/10.1021/jacs.8b07515.